Improved modeling of the Arctic halocline with a subgrid-scale brine rejection parameterization

A. T. Nguyen,[1] D. Menemenlis,[1] and R. Kwok[1]

[1] The halocline in the Arctic Ocean plays an important role in regulating heat exchange at the bottom of the mixed layer and it has a direct effect on the ocean sea ice energy balance and sea ice mass balance. Modeling the halocline, however, remains a challenge in current state-of-the-art coupled ocean sea ice models including those that participated in the Arctic Ocean Model Intercomparison Project. In this study, we successfully reproduce a cold halocline in the Canada Basin by implementing a subgrid-scale brine rejection parameterization in an ocean general circulation model. The brine rejection scheme improves the solution by redistributing surface salts rejected during sea ice formation to their neutral buoyancy depths. The depths are based on salt plume physics and published laboratory and numerical experiments. Compared with hydrographic data from 1993 to 2004, distribution of most of the rejected salt to the bottom of the mixed layer seems to yield the lowest model-data misfits. We also show that the model's mixed layer depth is sensitive to the background diffusivity ν used in the k-profile parameterization vertical mixing scheme. A background diffusivity of 10^{-6} m^2/s in combination with brine rejection scheme described herein yield the best simulation of the Arctic halocline.

1. Introduction

[2] The upper 1000m of the Arctic Ocean features a mixed layer from the surface down to approximately 50 m depth, a halocline with near freezing temperature and very high salinity gradient between approximately 50–200 m depth, and an Atlantic Water layer with temperature exceeding 0.5°C below 300 m [*Rudels et al.*, 2004]. Using hydrographic data from the Sea Ice Expedition (SCICEX) cruises, *Steele and Boyd* [1998] and *Boyd et al.* [2002] found that the halocline had retreated in the Eurasian Basin in the early 1990s and partially recovered in 1998–2000. In the Canada Basin, however, the halocline is still a prominent feature at depth ~50–250 m, as observed in conductivity-temperature-depth (CTD) casts from SCICEX cruises [*Rudels et al.*, 2004; *Steele and Boyd*, 1998] and from the Beaufort Gyre Experiment Project (BGEP) in 2003–2004 [*Kemp et al.*, 2005]. Without the halocline, heat from the Atlantic Water can get entrained into the mixed layer and melt significant amount of Arctic sea ice [*Steele and Boyd*, 1998]. Thus, the halocline plays a vital role in regulating heat input into the mixed layer from below, and has a direct effect on the ocean sea ice energy balance and sea ice mass balance [*Steele and Boyd*, 1998].

[3] Modeling a realistic halocline remains a challenge in current state-of-the-art coupled ocean sea ice models. In the Arctic Ocean Model Intercomparison Project (AOMIP), 10 state-of-the-art Arctic Ocean and sea ice models were compared with each other. All 10 models failed to reproduce the halocline partly due to lack of physics in vertical mixing process and/or shelf/basin exchanges (Figure 1 [*Holloway et al.*, 2007]). Specifically, all models produced a temperature gradient from depth ~50–200 m, in contrast to the near-freezing temperature observed between these depths in the Amerasian domain (Figure 1). A coupled ocean and sea ice configuration of the Massachusetts Institute of Technology general circulation model (MITgcm) produces a similar temperature gradient in the Arctic. In our initial investigation we found that excessive vertical mixing (1) destroys the steep salinity gradient associated with the halocline, (2) deepens the mixed layer depth (MLD), and (3) brings heat from the Atlantic Water to near the surface to create the observed temperature gradient.

[4] A similar problem with salinity gradient degradation was observed in ocean general circulation models in the Southern Ocean. *Duffy and Caldeira* [1997] and *Duffy et al.* [1999] showed that excessive vertical mixing destroyed the sharp pycnocline associated with the Antarctic Intermediate Water (AAIW). To address this issue, *Duffy and Caldeira* [1997] and *Duffy et al.* [1999] introduced a subgrid salt plume scheme to reduce grid-scale vertical mixing. *Duffy and Caldeira* [1997] justification for subgrid parameterization is that salt rejection occurs at ~1–10 km scale which is too small for global circulation models to resolve. In their parameterization, salt rejected from sea ice formation was distributed uniformly down to a depth of density 0.4kg/m^3 higher than the surface density. When they turned on the salt

---

[1]Jet Propulsion Laboratory, California Institute of Technology, Pasadena, California, USA.
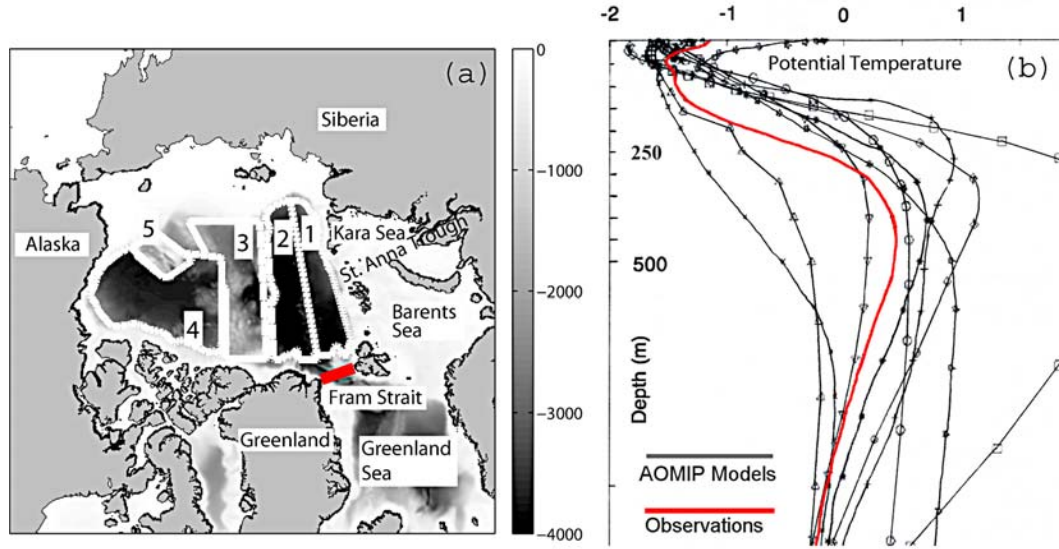
Figure 1. (a) Map of the Arctic Ocean showing the Nansen Basin (area 1), Amundsen Basin (area 2), Makarov Basin (area 3), Canada Basin (area 4), and Chukchi Cap (area 5). The gray color scale shows bathymetry in m. (b) AOMIP vertical temperature profiles in the Amerasian domain (black curves) compared to observation (red curve). Amerasian domain includes the Canada and Makarov basins and the Chukchi Cap. The halocline is the region between depth 50 and 200 m where temperature is near freezing and salinity gradient is high. In contrast to observation, AOMIP results show a temperature gradient from depth 250 m to the surface. Figure 1b is from *Holloway et al.* [2007].

plume scheme, the sharp salinity gradients associated with the AAIW in the model were preserved. In addition to reproducing the AAIW, they were also able to realistically simulated the North Atlantic Deep Water and the Antarctic Circumpolar Current. In this study, we implement a parameterization similar to *Duffy et al.* [1999] in a regional configuration of the MITgcm to improve the vertical salinity structure in the Arctic and to reproduce the halocline. Primary differences between our scheme and that of *Duffy et al.* [1999] include the criteria for determining the depth to which the rejected brine is mixed, and a salt vertical distribution function. Available conductivity-temperature-depth data are used to assess the model performance. In addition, we also investigate the effect of background diffusivity on vertical mixing.

[5] The outline of the paper is as follows. Section 2 summarizes the physics of brine mixing based on previous laboratory experiments and numerical studies of brine rejection during sea ice formation. The parameterization of brine rejection in our model is described in detail in section 3. Sections 4 and 5 describe the CTD data and model configuration and numerical experiments. In section 6 we present and discuss results of the sensitivity experiments to examine the modeled halocline of the Arctic Ocean. A summary of our findings and final remarks are in section 7.

2. Salt Plume Physics

2.1. Theory and Previous Laboratory Experiment Results

[6] Seasonal sea ice can retain up to 30% of the seawater salinity in brine pockets and melt frozen ponds and has salinity of about 10 [*Nakawo and Sinha*, 1981]. The remaining salt is rejected as brine into the ocean. Scaling analyses and laboratory experiments by *Morton et al.* [1956], *Scorer* [1957], *Helfrich* [1994], and *Bush and Woods* [1999] show that when salt is introduced into a density stratified fluid, the depth to which the salt penetrates and the horizontal extent of the salt distribution are controlled mainly by the initial buoyancy, the fluid stratification strength, and the fluid rotation rate. Assume that a point source plume is released from rest with a horizontal scale b and vertical extent z as shown in Figure 2, and let f be the Coriolis frequency, V_o the initial volume of the plume, ρ_o and ρ_a the initial salt plume and ambient densities, respectively, the initial salt plume buoyancy F_o in unit of m^4/s^2 is

$$F_o = V_o g \frac{\rho_o - \rho_a}{\rho_a}, \tag{1}$$

where g is the gravitational acceleration. The fluid density stratification is expressed, in terms of N, the Brunt-Väisälä frequency, as follows:

$$N^2 = -\frac{g}{\rho} \frac{d\rho}{dz}. \tag{2}$$

In the case $N/f \gg 1$ and where rotation is unimportant, *Morton et al.* [1956] showed that the rejected salt penetrates to a neutral buoyancy depth z_M and has a horizontal spread radius b_M described by

$$z_M \approx k_1 \left[F_o N^{-2} \right]^{1/4} \tag{3}$$
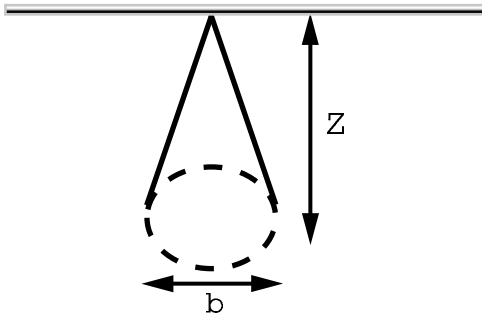
$$b_M \approx k_2 z_M. \tag{4}$$

Figure 2. Geometry of a salt plume originating from a point source, with horizontal and vertical length scales b and z, respectively [*Turner*, 1969].

Values of k_1 and k_2 are 2.66 and 0.25 based on scaling analyses [*Scorer*, 1957]. Laboratory experiments by *Helfrich* [1994] show that the salt plume overshoots z_M slightly, but stabilizes at this depth and begins to spread horizontally as an axisymmetric intrusion until time $t \sim f^{-1}$ when rotation becomes significant. The plume then breaks into small anticyclonic eddies and gets entrained into the surroundings [*Helfrich*, 1994].

[7] In the case where stratification $d\rho/dz$ is weak and rotation dominates, $N/f \ll 1$, the salt lateral growth is constrained to columns of radius b_R at an approximate depth z_R with time scale $t \sim f^{-1}$ [*Scorer*, 1957] such that

$$z_R \approx k_3 \left[F_o f^{-2} \right]^{1/4} \qquad (5)$$

$$b_R \approx k_4 z_R. \qquad (6)$$

Scaling analyses and experimental values for $[k_3, k_4]$ are [3.6, 0.25] and [4.94, 0.21], respectively [*Scorer*, 1957; *Helfrich*, 1994]. The salt column then continues to penetrate as a Taylor column of radius b_R until it reaches approximately the neutral buoyancy depth z_M where it breaks up into anticyclonic and cyclonic pairs of eddies due to geostrophic adjustment [*Helfrich*, 1994]. The transition between stratification-controlled and rotation-controlled regimes occurs at approximately $N/f \sim 0.6$ and is independent of the initial plume buoyancy F_o [*Helfrich*, 1994].

[8] When the plume source is 2-D and continuous for some finite time t_s, as is the case during lead openings and sea ice freezing [*Morison et al.*, 1992], the physics of the plume penetration remains similar to its 1-D counterpart, with some modifications [*Bush and Woods*, 1999]. In this case, the important parameters are the Coriolis frequency f, Brunt-Väisälä frequency N, the length scale of the line source L, and the plume buoyancy flux per unit length B_o. B_o depends on the volume flux per unit length Q_o (m^2/s) as follows:

$$B_o = Q_o g \frac{\rho_o - \rho_a}{\rho_a}. \qquad (7)$$

B_o has unit $[m^3/s^3]$. Again, the two cases to consider are when stratification dominates ($N/f \gg 1$) and when rotation

dominates ($N/f \ll 1$). For most oceanic applications, the first case, $N/f \gg 1$, is most relevant and will be covered here [*Bush and Woods*, 1999]. The neutral buoyancy depth z_M to which the 2-D salt plume penetrates is derived from laboratory experiments by *Bush and Woods* [1999] as follows:

$$z_M \approx (3.0 \pm 1.0) \frac{B_o^{1/3}}{N}. \qquad (8)$$

After reaching z_M, the 2-D salt plume spreads horizontally until time $t \sim f^{-1}$ when it breaks up into multiple anticyclonic vortexes with characteristic radii that scale with B_o and t_s.

2.2. Previous Numerical Modelings and Field Studies

[9] The 2-D experiment in section 2.1 provides insights into how rejected salt mixes under leads. Winter leads are openings due to divergence of sea ice, and have typical length scales of $50-1000$ m in width and $1-50$ km in length [*Morison et al.*, 1992]. The large heat exchange between the relatively warm water and very cold air $-15°C$ to $-20°C$ results in rapid sea ice formation and brine rejection. Data from the 1974 Arctic Ice Dynamics Joint Experiment [*Smith*, 1974; *Morison*, 1978], the 1976 Arctic Mixed Layer Experiment [*Morison et al.*, 1992], and the 1992 Lead Experiments [*Muench et al.*, 1995; *Morison and McPhee*, 1998] show that when the ice velocity is less than $\sim$0.10 m/s, the following processes as shown in Figure 3 are consistently observed. Salt plumes first form at the edges of the lead, then sink to the bottom of the mixed layer and spread out horizontally away from the lead axis (see black vertical arrows in Figure 3). At the surface, returning flows advect freshwater horizontally toward the lead center (gray horizontal arrows in Figure 3). When ice velocity is large,
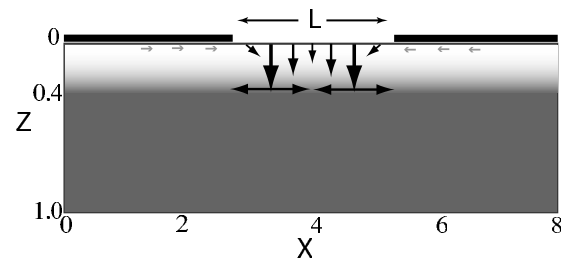

Figure 3. Schematic drawing of a 2-D lead convection of *Kozo* [1983] and *Smith and Morison* [1998] numerical models. Units in x direction and z direction are normalized by the total depth of the domain. Heavy black lines at $z = 0$ represent sea ice which can move in the x direction relative to the ocean. Typical values for mixed layer depth are $\sim$15–40 m, and for lead width L are $\sim$50–1000 m. A halocline at depth $z = 0.4$ is qualitatively shown with the gray scale. *Smith and Morison* [1998] results are qualitatively summarized here with black arrows for salt plumes and gray horizontal arrows for ocean return flows near the surface. The salt plumes first form at the lead's edges, then sink to the bottom of the mixed layer and spread horizontally (see also plate 3 of *Smith and Morison* [1998]).

turbulent forces dominate and distribute the brine throughout the mixed layer.

[10] The lead-induced salt plume convections are well reproduced in numerical models [*Kozo*, 1983; *Smith and Morison*, 1993, 1998; *Smith et al.*, 2002]. *Kozo* [1983] and *Smith and Morison* [1998] modeled brine rejection in a 2-D domain of size ∼2500 m wide by 100 m deep with a lead 750 m wide at the center (Figure 3). A halocline of gradient $d\rho/dz \sim 0.005$ kg/m^3/m is placed at 40m depth. As sea ice begins to form at the edges of the lead, plumes of sizes comparable to the lead's width sink to the bottom of the mixed layer, then spread out horizontally away from the lead center [*Smith and Morison*, 1998]. The vertical salt flux they observed of $\sim 5 \times 10^{-5}$ kg/m^2/s and salinity disturbances $\Delta S \sim 0.01-0.02$ are consistent with observations. In one experiment, salt plumes weakly penetrate the halocline. However, this is only the case when the buoyancy force is very high and there is no relative ice-ocean velocity at the surface. Rotation does not play an important role in salt plume convection in the Arctic because the halocline is at too shallow depth (~ 40 m) compared to the depth required for rotational effect ($\sim 3000-4500$ m [*Smith et al.*, 2002]).

[11] In summary, both numerical models and field observations show consistent patterns of buoyancy convection associated with brine rejection beneath leads. The plume sinks to the bottom of the mixed layer, but cannot penetrate the halocline. Instead, it spreads horizontally along the top of the halocline, and reduces the depth of the mixed layer [*Morison et al.*, 1992]. The horizontal extent of salt plume convection is of the order ~ 3 times the width of the lead [*Smith and Morison*, 1998]. Given that typical lead widths are $\sim 50-1000$ m, buoyancy convection will have typical horizontal extent of $\sim 100-3000$ m. Most global ocean models cannot resolve convection at this horizontal length scale [*Duffy and Caldeira*, 1997]. As a result, the rejected salt at the surface is spread across the entire grid which in turn causes instability and large-scale convection in the mixed layer. Large-scale convection in turn deepens the mixed layer in contrast to observations, laboratory and numerical experiment results [*Morison et al.*, 1992; *Helfrich*, 1994; *Smith and Morison*, 1998; *Duffy and Caldeira*, 1997]. In section 3, we discuss the implementation of a subgrid salt rejection scheme to address this large grid-scale convection problem.

3. Salt Plume Parameterization in our MITgcm Configuration

3.1. Brine Rejection Treatment

[12] As mentioned earlier, *Duffy and Caldeira* [1997] and *Duffy et al.* [1999] introduced subgrid brine rejection parameterization to reproduce the sharp salinity gradients associated with the AAIW in the Southern Ocean, and their success motivated us to implement a similar scheme for the Arctic Ocean. In our model, sea ice retains 30% of the top layer's salinity during freezing. The remaining salt (70%) is rejected back to the ocean. *Duffy et al.* [1999] distributed the salt uniformly from the surface down to a depth with density $0.4 kg/m^3$ greater than the surface density ρ_{surf}. The value of $\Delta \rho = 0.4 kg/m^3$ was chosen to best fit their model results to observations in the Southern Ocean. In place of the uniform distribution, here we introduce a simple depth-dependent

distribution function of salt $s(z)$ and the corresponding cumulative function $S(z)$ as follows:

$$s(z) = \begin{cases} Az^n & \text{if } |z| \leq |D_{sp}| \\ 0 & \text{if } |z| > |D_{sp}| \end{cases} \quad (9)$$

$$S(z) = \int_0^z s(z')dz'. \quad (10)$$

Here n and D_{sp} are the distribution power and salt plume depth, respectively, and are adjustable parameters. $S(z)$ is the cumulative salt as a function of depth z, with $S(z = D_{sp})$ constrained to equal to the total amount of rejected salt S_o. The constant $A = (n + 1)/D_{sp}^{(n+1)}$ is determined using the above constraint of $S(z = D_{sp}) = S_o$. Figure 4 shows the distribution functions for $n = [0-7]$. *Duffy et al.* [1999] used a criterion $\Delta \rho = \rho(z) - \rho_{surf} = 0.4 kg/m^3$ to determine D_{sp}, then set $n = 0$ which yielded $s(z) = A = 1/D_{sp}$ for a uniform distribution (Figure 4, dark blue curve).

[13] Based on the laboratory and numerical experiment results discussed in section 2, most of the salt reaches the bottom of the MLD instead of mixing down uniformly. To determine D_{sp}, we locate the depth immediately below the mixed layer and above the halocline. The k-profile parameterization (KPP) scheme, based on a bulk Richardson number criterion, calculates an oceanic boundary layer (OBL) depth, which is the depth of active mixing. The mixed layer depth (MLD) depends on the time history of mixing and can be deeper or shallower than the OBL depending on definition. *Lukas and Lindstrom* [1991] discussed the various definitions of MLD based on observed density, temperature, and salinity gradient criteria and concluded that the most reliable criterion was density gradient for an upper ocean with a steep pycnocline. In our case, with the high-salinity gradient in the halocline, we also use a $d\rho/dz$ instead of a $\Delta \rho$ as used by *Duffy et al.* [1999] to determine the MLD. A density gradient criterion is technically the same as a salinity gradient criterion in the Arctic Ocean because of the near-freezing temperature in the upper ocean. A MLD calculated as described here correlates well with the KPP OBL but is typically deeper than the KPP OBL by $5-10$ m.

[14] In the mixed layer, density is relatively uniform with $d\rho/dz \approx 0$. In the halocline, typical density gradients are of the order $d\rho/dz \approx [0.01, 0.02]$ kg/m^3/m. We used two pairs of sensitivity experiments to optimize for the values of n and $d\rho/dz$ in equation (9) using a Green's Function approach [*Menemenlis et al.*, 2005]. In the first pair of experiments, initial guesses of $n = 1$ and $n = 2$ are used with $d\rho/dz = 0.005$. In the second pair, initial guesses of $d\rho/dz = 0.005$ and $d\rho/dz = 0.01$ are used with $n = 2$. To assess the results, we defined a cost function J as the sum of squares of residuals of model minus data of all available density vertical profiles as calculated from temperature and salinity (T/S) profiles. If we assign variables $\alpha = [d\rho/dz, n]$ and calculate J for the above four sensitivity experiments, the gradients $\partial J/\partial \alpha$ can be used to find optimal values for α as used by *Menemenlis et al.* [2005]. These optimal values are $d\rho/dz = 0.02$ and $n = 5$. D_{sp} is then set to the depth which corresponds to the density gradient of 0.02 kg/m^3/m. The
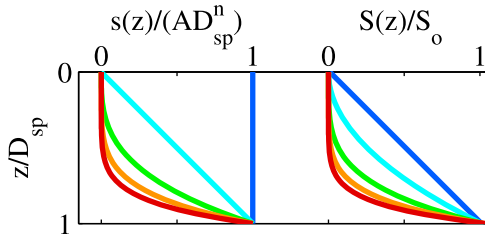
Figure 4. (left) Normalized distribution $s(z)$ and (right) cumulative salt $S(z)$ as a function of depth z and power n. Here the n values are [0,1,3,5,7] with colors progressively changing from $n = 0$ in blue to $n = 7$ in red. *Duffy et al.* [1999] used $n = 0$ to produce a uniform distribution $s(z)$. At higher n, more salt is taken from the surface and distributed at D_{sp}. $S(z)$ is the total accumulation at depth, such that at $z = D_{sp}$, $S(z) = S_o$, where S_o is the amount of salt rejected during sea ice formation.

optimized value $n = 5$ is significantly higher than the value $n = 0$ used by *Duffy et al.* [1999]. Specifically, changing from $n = 0$ and $d\rho/dz = 0.005$ to $n = 5$ and $d\rho/dz = 0.02$ results in a 35% reduction in the cost J.

[15] Figure 5 shows maps of the MLD as calculated using the $d\rho/dz = 0.02$ kg/m^3/m criterion and the 14 year mean MLD seasonal cycles for experiments with and without the salt plume scheme. Based on the time series in Figure 5e, MLD reaches its deepest depth during February. As a result, February monthly mean MLD are used here for comparison between the experiments. The MLD for February 1992 (Figure 5a), which is very close to initial conditions, is between 20–40 m. In late Fall to early Winter (September–December), brine rejection during sea ice formation deepens the MLD in all cases by 10–20 m. From January to May, the MLD continues to deepen by ∼5 m when the salt plume scheme is not used (Figures 5b and 5c, solid lines in Figure 5e). In contrast, when the scheme is used, the MLD only increases by 0–2 m (dashed lines in Figure 5e). If we define shoaling as the depth difference between the end of winter minus beginning of winter for experiments without and with the salt plume scheme, i.e., ∼5 m without and 0–2 m with salt plume, then the shoaling effect due to the salt plume scheme is ∼3–5 m.

3.2. Brine Rejection With KPP Vertical Mixing

[16] Our configuration of the MITgcm uses the KPP from *Large et al.* [1994] to calculate vertical mixing in the Oceanic Boundary Layer (OBL) and in the deep ocean. The OBL depth is determined using a local bulk Richardson number Ri_b and a critical bulk Richardson number Ri_{cr} criterion. Ri_b is roughly defined as $Ri_b(z) \sim z\Delta B/\Delta V^2$, where z is depth, ΔB is the differential buoyancy between near surface and bottom of mixed layer, and ΔV^2 the differential shear (Figure 6). An increase in ΔB implies a sharper density gradient with depth, hence a steeper $Ri_b(z)$ (compare curve 2 to curve 1 in Figure 6). On the other hand, when there is increasing differential shear ΔV^2, $Ri_b(z)$ will be shallower (curve 3 in Figure 6). For a given Ri_{cr}(dashed black line in Figure 6), the location where $Ri_b(z)$ crosses Ri_{cr} defines approximately the depth of the OBL in the KPP scheme. Thus, for an increase in ΔB and ΔV, the mixing

layer is shallower ($z_{\Delta B}$ in Figure 6) and deeper ($z_{\Delta V}$ in Figure 6), respectively.

[17] When the salt plume scheme is turned on, rejected salt is removed from the surface and added to the bottom of the mixed layer. As a consequence, salinity and density gradients and ΔB are higher than in the case when salt plume is turned off. This results in a shallower OBL depth when the salt plume scheme is used (curve 2 in Figure 6).

4. Data

[18] Observational data used to assess the proposed sub-grid-scale parameterization are conductivity-temperature-
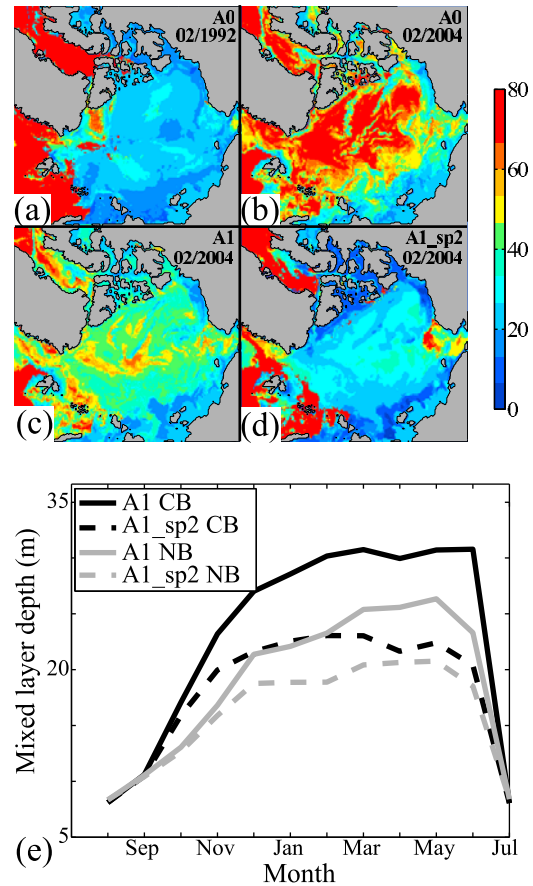

Figure 5. Mixed layer depth in m in (a) February 1992 for all experiments, (b) February 2004 for **A0**, (c) February 2004 for **A1**, (d) February 2004 for the experiment with salt plume scheme turned on **A1_sp2**, and (e) 1992–2004 mean annual mixed layer depth in the Canada (black) and Nansen (gray) basins for experiments **A1** (solid) and **A1_sp2** (dashed). In the baseline experiment **A0**, the MLD is too deep compared to observations and causes the cold halocline to degrade. Decreasing the KPP background diffusivity (Figure 5c) and/or using the salt plume scheme (Figure 5d) result in shallower MLD. The seasonal cycle shows the deepening of the MLD in late fall to early winter (September–December) as brine is rejected during sea ice formation. From January to May, the MLD continues to deepen by ∼5 m in **A1** (solid lines in Figure 5e), whereas in **A1_sp2**, the MLD shoals with small MLD increases of ∼0–1 m over the winter season.
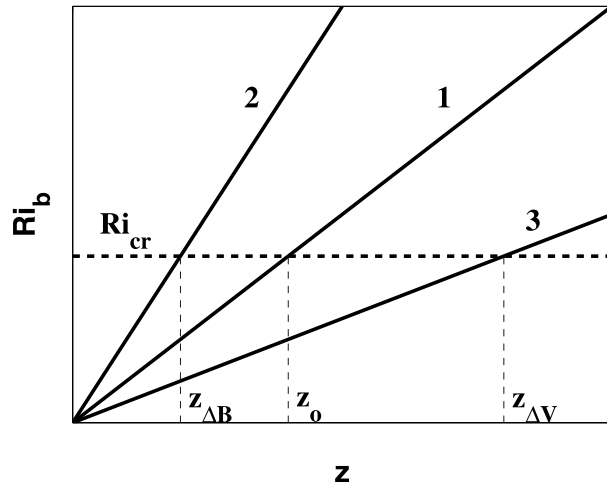
Figure 6. Schematic plot of the local bulk Richardson number Ri_b in the oceanic boundary layer, as defined in the KPP vertical mixing scheme, as a function of depth z. Curves 1–3 represent a reference case (curve 1), a case with increased buoyancy difference between the surface and at the bottom of the mixing layer (curve 2), and a case with increased differential shear velocities (curve 3). For a given critical bulk Richardson number Ri_{cr}, locations z_o, $z_{\Delta B}$, and $z_{\Delta V}$ define the oceanic boundary layer depth for the three cases, respectively. Values of z are relative, with $z_{\Delta B} < z_o < z_{\Delta V}$.

depth measurements from the Scientific Ice Expeditions (SCICEX [*Langseth et al.*, 1993; *Hopkins et al.*, 1998; *Boyd et al.*, 1998; *Edwards et al.*, 1999; *Rothrock et al.*, 1999]) and the Beaufort Gyre Exploration Project (BGEP [*Kemp et al.*, 2005]). The data span the years 1993–2000 for SCICEX and 2003–2004 for BGEP data. Single measurement accuracies range from ±0.001 to ±0.005°C for temperature and approximately ±0.005 for derived salinity (http://www.seabird.com, http://falmouth.com). Data are downloaded from http://www.ldeo.columbia.edu/, http://nsidc.org, and http://www.whoi.edu/beaufortgyre/. Figure 7 shows the spatial distribution of the data in the four basins in the Arctic and in the Chukchi Cap area.

5. Numerical Sensitivity Experiments

[19] To reduce computational cost, we use a regional Arctic Ocean configuration of the MITgcm global grid. The model has horizontal resolution of ∼18 km and 50 vertical levels. Surface forcings are from ERA-40 and ECMWF. Boundary conditions are monthly and are taken from the Estimating the Circulation and Climate of the Ocean, Phase 2 (ECCO2) global optimized solution [*Zhang et al.*, 2008; *Menemenlis et al.*, 2008]. Initial conditions are from the World Ocean Atlas 2005 [*Antonov et al.*, 2006; *Locarnini et al.*, 2006] starting in January 1992. Initial sea ice condition is from *Zhang and Rothrock* [2003]. The model is allowed to run until the end of October 2006. No climate restoring is used.

[20] A set of nine experiments as shown in Table 1 is performed. The baseline, **A0**, is taken from the global optimized ECCO2 solution as described above. The rest

of the experiments use parameters from **A0**, but with changing KPP background diffusivity ν and with the salt plume scheme turning on or off. Experiments **A1** and **A2** are background diffusivity sensitivity experiments. *Zhang and Steele* [2007] showed that their regional model with a KPP background diffusivity $\nu \sim 10^{-6}$ m²/s (ν_s^w [*Large et al.*, al.*, 1994]) in the Arctic reproduced the most realistic Atlantic Water layer and circulation. Compared to observations, *Zhang and Steele* [2007] showed that further decrease of ν in combination with KPP being turned off resulted in unrealistic build up of fresh water at the surface and build up of heat in the halocline as well as too shallow mixed layer depth. Here we investigate the sensitivity of the upper ocean in the Arctic to both ν and salt rejection. The next sets of experiments, **A[0-2]_sp1** and **A[0-2]_sp2** are sensitivity experiments with the salt plume scheme turned on using $d\rho/dz = 0.01$ and $d\rho/dz = 0.02$ criteria. The two $d\rho/dz$ criteria are used to investigate the spatial variation of the mixed layer depth in the Amerasian and Eurasian Basins. In all experiments, tracer transport equations are solved using a high-order monotonicity preserving scheme [*Daru and Tenaud*, 2004]. The implicit diffusivity associated with this advection scheme is in the range of 10^{-7} to 10^{-6} m²/s. Here we calculated numerical diffusion by first diagnosing net vertical transports (advective plus numerical diffusive) and
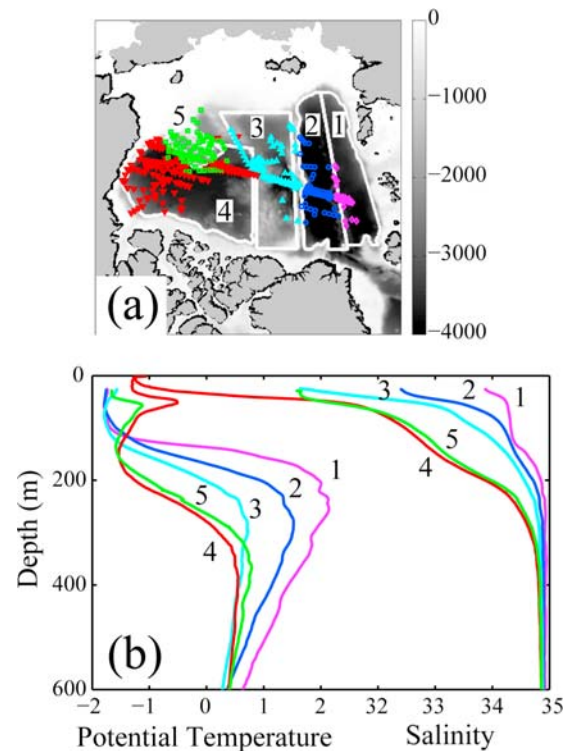

Figure 7. (a) Locations of data in the Nansen Basin (purple, area 1), Amundsen Basin (dark blue, area 2), Makarov Basin (light blue, area 3), and Canada Basin (red, area 4), and Chukchi Cap (green, area 5). (b) Typical vertical temperature and salinity profiles in the basins and Chukchi Cap based on observations. Colors and numbers correspond to the basins as identified in Figure 7a. Temperature is in °C. The gray color scale shows bathymetry in m.

Table 1. List of Experiments[a]

Salt Plume	$\nu = 10^{-5}$ m²/s	$\nu = 10^{-6}$ m²/s	$\nu = 0$ m²/s
Off	A0	A1	A2
sp1	A0_sp1	A1_sp1	A2_sp1
sp2	A0_sp2	A1_sp2	A2_sp2

[a]Salt plume experiments sp1 and sp2 use values of $d\rho/dz = 0.01$ kg/m³/m and $d\rho/dz = 0.02$ kg/m³/m, respectively. Two $d\rho/dz$ criteria are used to investigate the spatial variation of the MLD in the various basins of the Arctic Ocean. Here ν is the background diffusivity used in the KPP vertical mixing scheme.

vertical advective transports of tracers, then calculating numerical diffusion as the difference between the net and advective transports. The numerical diffusion is typically in the range of 0−5% of the net vertical transports in the upper 150m (excluding the mixed layer where diffusion of uniform tracers is not a concern.)

6. Results and Discussion

[21] Figure 7 shows the geographic locations of the Nansen (purple, 1), Amundsen (dark blue, 2), Makarov (light blue, 3), Canada Basins (red, 4) and Chukchi Cap (green, 5), as well as CTD data distribution and typical vertical salinity/temperature profiles within each region based on observations. The halocline is most distinctive in the Canada Basin and Chukchi Cap, extending down to depth >250 m (Figure 7b, curves 4 and 5), and is progressively shallower in the Makarov (curve 3) and Amundsen

Basins (curve 2). In the Nansen Basin, the halocline is entirely missing (low-salinity gradient in curve 1), and the mixed layer extends down all the way to the top of the Atlantic Water [Rudels et al., 2004]. The Atlantic Water, roughly defined as water with temperature > 0°C, transitions from warmer and shallower in the Nansen Basin to cooler and deeper in the Canada Basin (curves 1−4 for temperature in Figure 7b).

[22] As mentioned in section 1, AOMIP and our models fail to reproduce the large salinity gradient and near freezing temperature observed in the halocline (Figure 1). Here, we assess the effectiveness of the subgrid brine rejection scheme on vertical mixing and on the reproduction of the halocline in the individual basins and in the Chukchi Cap area. For the Canada and Makarov Basins and Chukchi Cap, a minimum of ten CTD locations is used each year to obtain model-data misfits and statistics. In the Amundsen and Nansen Basins where data are sparse, a minimum of five CTD locations is used for assessment calculations. All pairs of temperature and salinity profiles are converted to density profiles. Note that in the upper Arctic Ocean, where temperature is near freezing, density is mainly a function of salinity. To measure the sensitivity experiments' improvements relative to the baseline, we first compute the sum of squares of residuals (SSQ) of model minus data, then calculate the percentage of improvement I as follows:

$$I = \frac{(\text{SSQ}_{\text{baseline}} - \text{SSQ}_{\text{sensitivity}})}{\text{SSQ}_{\text{baseline}}} \times 100. \quad (11)$$

Table 2. Percentage of Improvements I[a]

		Canada Basin				Chukchi Cap				Makarov Basin				Amundsen Basin				Nansen Basin			
			ν (m²/s)				ν (m²/s)				ν (m²/s)				ν (m²/s)				ν (m²/s)		
Data	Salt Plume	M	10^{-5}	10^{-6}	0	M	10^{-5}	10^{-6}	0	M	10^{-5}	10^{-6}	0	M	10^{-5}	10^{-6}	0	M	10^{-5}	10^{-6}	0
sc93	off	5	–	–	–	0	–	–	–	4	–	–	–	4	–	–	–	0	–	–	–
	sp1	5	–	–	–	0	–	–	–	4	–	–	–	4	–	–	–	0	–	–	–
	sp2	5	–	–	–	0	–	–	–	4	–	–	–	4	–	–	–	0	–	–	–
sc95	off	28	0	32	24	2	–	–	–	26	0	17	15	13	0	11	9	5	0	14	11
	sp1	28	27	16	12	2	–	–	–	26	19	21	20	13	35	38	34	5	7	14	14
	sp2	28	28	12	7	2	–	–	–	26	32	32	30	13	55	53	51	5	−4	−6	−4
sc96	off	25	0	11	11	34	0	−11	−13	16	0	18	18	4	–	–	–	2	–	–	–
	sp1	25	−1	−14	−19	34	−6	−22	−20	16	20	21	23	4	–	–	–	2	–	–	–
	sp2	25	−7	−25	−31	34	−5	−21	−25	16	22	22	23	4	–	–	–	2	–	–	–
sc97	off	43	0	38	38	6	–	–	–	29	0	22	27	8	0	−53	−90	2	–	–	–
	sp1	43	29	28	24	6	–	–	–	29	23	22	26	8	39	20	7	2	–	–	–
	sp2	43	28	24	20	6	–	–	–	29	30	30	31	8	77	70	50	2	–	–	–
sc98	off	16	0	32	33	15	0	24	22	48	0	53	61	15	0	19	14	9	0	9	−26
	sp1	16	16	25	24	15	7	11	4	48	12	45	53	15	16	34	33	9	56	79	71
	sp2	16	9	26	22	15	−6	9	2	48	14	54	61	15	32	50	51	9	44	64	73
sc99	off	31	0	44	44	16	0	13	−7	12	0	22	24	18	0	−10	−14	7	0	−6	−16
	sp1	31	23	44	44	16	9	19	−4	12	19	28	36	18	28	36	27	7	75	78	72
	sp2	31	25	42	41	16	−7	19	4	12	26	37	41	18	45	43	39	7	76	78	79
sc00	off	24	0	10	4	0	–	–	–	14	0	54	61	5	0	23	26	5	0	61	49
	sp1	24	7	5	−1	0	–	–	–	14	52	65	65	5	58	83	82	5	86	89	84
	sp2	24	6	7	2	0	–	–	–	14	63	79	76	5	67	79	79	5	85	88	87
bgep03	off	26	0	69	75	10	0	32	15	0	–	–	–	0	–	–	–	0	–	–	–
	sp1	26	36	70	73	10	18	34	16	0	–	–	–	0	–	–	–	0	–	–	–
	sp2	26	45	75	74	10	16	32	12	0	–	–	–	0	–	–	–	0	–	–	–
bgep04	off	28	0	33	32	0	–	–	–	0	–	–	–	0	–	–	–	0	–	–	–
	sp1	28	28	33	26	0	–	–	–	0	–	–	–	0	–	–	–	0	–	–	–
	sp2	28	46	53	43	0	–	–	–	0	–	–	–	0	–	–	–	0	–	–	–

[a]M is the number of CTD profiles available for each year. Here sc93−sc00 are SCICEX data for 1993−2000 and bgep03 and bgep04 are BGEP data for 2003−2004. Values listed here are percentage of improvement I in the sum of squares of residuals (equation (11)).
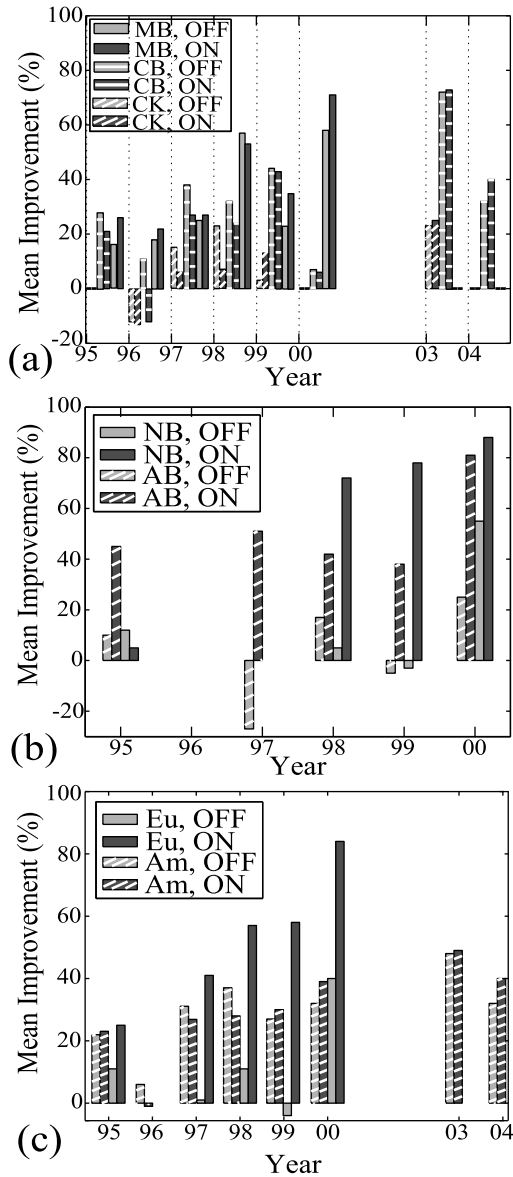
Figure 8. Mean improvements as a function of time for (a) Canada Basin (CB), Makarov Basin (MB), and Chukchi Cap (CK); (b) Amundsen Basin (AB) and Nansen Basin (NB); and (c) the Eurasian Basin (Eu) and Amerasian Basin (Am) with the salt plume scheme off (light gray) and on (dark gray). The improvements between on and off cases are comparable in the Amerasian Basin (Figures 8a and 8c). In the Eurasian Basin, however, the on case consistently yields higher improvements (Figures 8b and 8c).

I is positive when the sensitivity experiment fits CTD observations better than the baseline, i.e., SSQ_sensitivity < SSQ_baseline, and negative when the fit is worse, i.e., SSQ_sensitivity > SSQ_baseline. **A0** is the baseline and **A[1-2]** and **A[0-2]_sp[1-2]** are sensitivity experiments. At each CTD location, the whole water column instead of only the upper ocean is used to calculate SSQ because we want to ensure that the salt plume scheme is penalized if it destroys the Atlantic Water and deep ocean water structures. Outliers in the data are removed to ensure I is not dominated by a few large residual points.

[23] Improvements for all the years when CTD data are available, 1993–2004, are shown in Table 2. To summarize the results from Table 2, we averaged improvements into two categories corresponding to when the salt plume scheme is "off" or "on." Decreasing ν from the **A0**'s value improves the results in 75% of the periods listed in Table 2. As a result, for each year, we average the two highest improvements among the experiments **A[0-2]** to obtain mean improvements for the off case. For the on case, we average the four highest improvements among the experiments **A[0-2]_sp[1, 2]**. As an example, from Table 2 for 1995, the improvements corresponding to off and on for the Canada Basin are (32 + 24)/2 = 28 and (27 + 16 + 28 + 12)/4 = 21, respectively. Figure 8 shows the results for off and on cases for all the basins and also for the combined Amerasian (Canada, Chukchi Cap, and Makarov) and Eurasian (Amundsen and Nansen) Basins.

[24] In sections 6.1–6.4, profiles are shown when CTD data are available. In the Canada Basin and Chukchi Cap areas, data from BGEP were collected in August 2003 and 2004. In the other basins, the latest available data, from SCICEX-00 expedition, were collected in October 2000.

6.1. Canada Basin and Chukchi Cap

[25] In the Canada Basin and Chukchi Cap, experiments with reduced background diffusivity (**A1**, **A2**) give similar improvements I as those with salt plume schemes (**A0_sp1**, **A0_sp2**, Table 2 and Figure 8a). Small ν values reduce the model's vertical mixing and prevent MLD deepening. The salt plume scheme affects the MLD in a similar way. When there is an excess of rejected salt, the scheme mixes the salt down at subgrid level, thus decreases the likelihood of large grid-scale vertical mixing and prevents the deepening of the mixed layer (compare Figures 5c and 5d). In the 14 year model integration period, there is a consistent shift in pattern of improvements with the on case yielding smaller improvements before 1999–2000 (1999 for Chukchi Cap, 2000 for Canada Basin) and larger improvements after 1999–2000. Specifically, experiments with the salt plume scheme can reproduce and maintain both the warm summer and cold winter Pacific waters better (Figures 9b and 10b). In the Amerasian Basin, the shift of the improvement patterns is more pronounced and implies large spatial scale improvements in the vertical density structures of the water masses (Figure 8c).

6.2. Makarov Basin

[26] The biggest improvements in the Makarov Basin are in salinity gradients between 50–200 m, and temperature in the Atlantic Water layer (Figure 11). At the surface, temperature is warmer than observed when ν is decreased and/or when the salt plume scheme is turned on. The baseline experiment **A0** has temperature closest to the observations between depths 0–100 m (dark blue curve in Figure 11 (top)), but does not have the correct physics: Based on the low-salinity gradients within these depths in **A0**, the approximate constant temperature suggests a mixed layer depth of ~100 m that is not observed in the salinity data (compare S profiles between dark blue and black dashed curves in Figure 11). At close to freezing temperature, density is a strong function of salinity and is practically independent of temperature (see contour lines in Figure 11
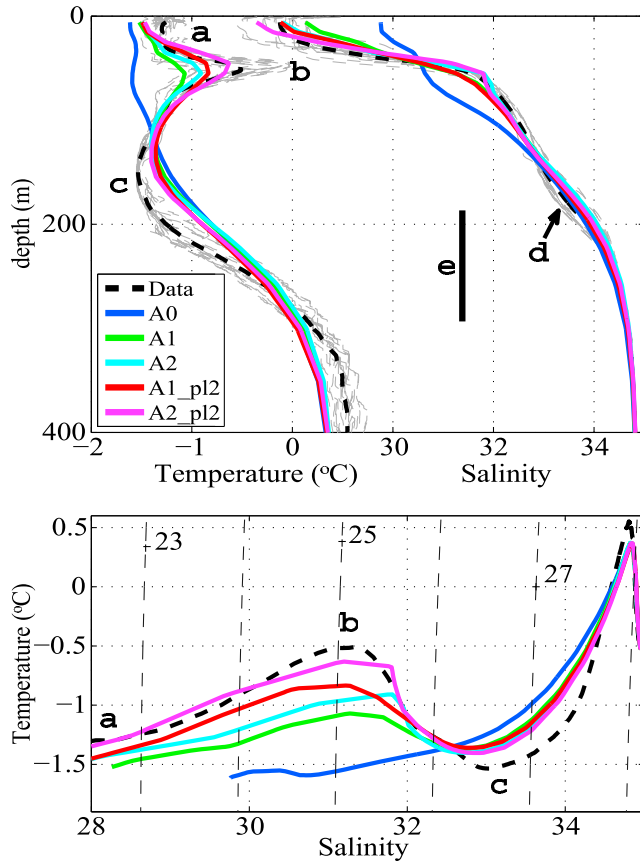
Figure 9. (top) Vertical temperature and salinity structures and (bottom) T/S diagram of the Canada Basin in August 2003 for the experiments listed in Table 1. In Figure 9 (top), the actual CTD measurements are shown in gray, with the data mean shown in dashed black. Additional annotations are mixed layer (point a), summer Pacific Water source (point b), winter Pacific Water source (point c), and salinity break indicating halocline of Pacific origin above (point d) and Atlantic origin below (point e, vertical bar [*Rudels et al.*, 2004]). Dashed contours in Figure 9 (bottom) are density anomaly.

(bottom)). As a result, decreased misfits in salinity have more physical significance than in temperature. With the salt plume scheme turned on, rejected salt at the surface is redistributed to greater depth, resulting in higher-salinity gradients and better fit to the observations (Figure 11, compare S profiles of **A[1-2]_sp[1-2]** to those of **A[1-2]** and to data). Except 1998, improvements in the on case are higher than in the off case for all the years when data are available (Figure 8a).

6.3. Amundsen Basin

[27] T/S profiles in the Amundsen Basin are similar to those in the Makarov Basin. However, reduction in model-data misfits in the Atlantic Water temperature and salinity gradients in the upper 200 m for the on case is more prominent in the Amundsen Basin. As a result, improvements are significantly higher for all the years when data are available (Figure 8b). At the surface, salinity becomes fresher by more than 2 when ν is decreased (Figure 12 (top)). With the salt plume scheme, salinity gradient

increases without becoming fresher than **A[1-2]** at the surface (Figure 12 (top)).

6.4. Nansen Basin

[28] In the Nansen Basin, the halocline is almost entirely missing and the mixed layer extends down to near the top of the Atlantic Water layer (Figure 7b, curve 1 [*Rudels et al.*, 2004]). Data in this basin are sparse, with less than 10 profiles per year (Table 2, Nansen Basin data). Salt plume experiments **A[0-2]_pl[1-2]** fit salinity and temperature observations reasonably in the Atlantic Water layer (Figure 13). However, all nine experiments fail to reproduce the deep mixed layer in the top 150 m. The good fit in temperature at depths ∼0−50 m between experiments **A[0-2]** and data are again questionable because **A[0-2]**'s near surface high-salinity gradients and low salinity (see also **A1**'s shallow MLD in Figure 5e). In general, experiments without the salt plume scheme yield salinity gradients that are higher and surface salinity that are fresher by 2−3 compared to observations. With the salt plume scheme, surface salinity is more realistic with values in the range of 32.3−33 (see right inset in Figure 13 (top)). Overall, in the Eurasian Basin (Amundsen and Nansen Basins combined), improvements
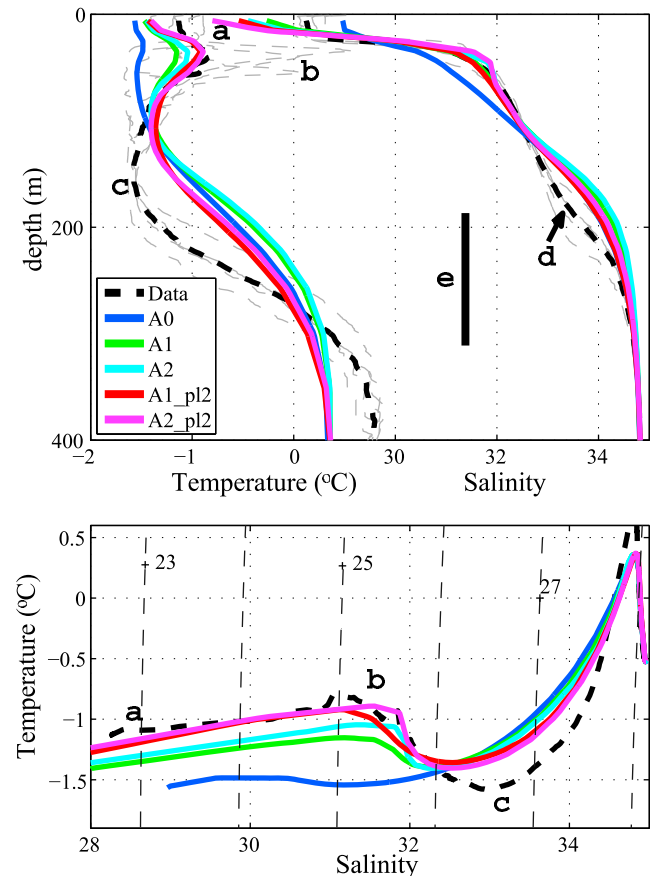

Figure 10. (top) Vertical temperature and salinity structures and (bottom) T/S diagram of the Chukchi Cap region in August 2003 for the experiments listed in Table 1. In Figure 10 (top), the actual CTD profiles are shown in gray, with the mean shown in dashed black. Annotations a–e are the same as in Figure 9. Dashed contours in Figure 10 (bottom) are density anomaly.
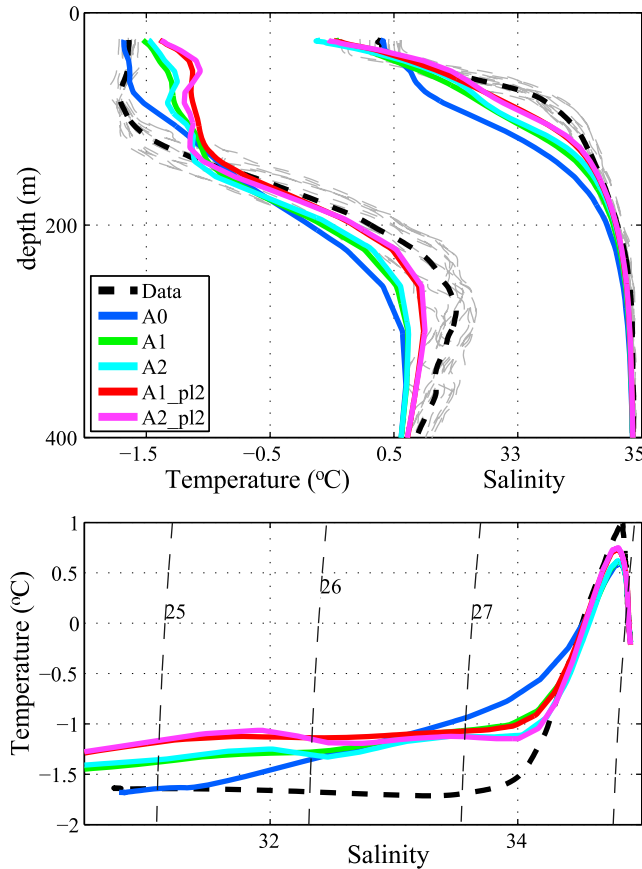
Figure 11. October 2000 vertical temperature and salinity structures in the Makarov Basin for the experiments listed in Table 1. (top) The actual CTD profiles are shown in gray, with the mean shown in dashed black. (bottom) Dashed contours are density anomaly.

in the cases when the salt plume scheme is on are more than twice the improvements in the off cases (Figure 8c).

[29] One possible reason for the large misfits in the Nansen Basin is the model's inability to reproduce the incoming Atlantic Water across Fram Strait [*Nguyen et al.*, 2008]. In our baseline solution **A0**, the Atlantic Water along the Fram Strait branch of the Norwegian Atlantic Current is deeper, thicker, and significantly colder than observed. As a consequence, the water flowing into the Arctic Ocean through Fram Strait does not have the correct properties, and results in lower volume and heat transports across Fram Strait compared with observations [*Nguyen et al.*, 2008]. After entering the Arctic Ocean through Fram Strait and the St. Anna Trough (see Figure 2 for locations), Atlantic Water mixes with surface melt water and flows along the Siberian side into the western Arctic Ocean (Canada Basin and Chukchi Cap combined [*Rudels et al.*, 2004]). Upon reaching the western Arctic, this water submerges beneath water of Pacific origin to form the lower halocline ("e" in Figure 9, [*Steele and Boyd*, 1998]). Due to problems with simulated inflow Atlantic Water in our model, the lower halocline in the western Arctic Ocean cannot be realistically reproduced in the experiments presented here (Figures 9 and 10, vertical bar and point e).

[30] Another possible reason for the large misfits is the highly stratified upper ocean, which results from the low background diffusivity values and from the salt plume scheme. Specifically, a decreased ν can precondition the ocean stratification in such a way as to inhibit episodic vertical mixing in the mixed layer. As a result, the top layers in the model become highly stratified with the mixed layer depth approaching the surface, consistent with results reported by *Zhang and Steele* [2007]. The shallow MLD can be seen in the 14 year annual mean MLD cycle in Figure 5e where in the Nansen Basin, the mean MLD is between 20 and 25 m for **A1** and between 18 and 20 m for **A1_sp2** over the winter.

6.5. Salt Plume Parametrization and Heat Budget

[31] One concern we have is the heat buildup in the Nansen and Amundsen Basins when the salt plume scheme is used (T profiles in Figures 12 and 13). Results of heat budgets for the Amerasian (Canada, Makarov, Chukchi Cap) and Eurasian (Amundsen and Nansen) Basins and the Greenland-Norwegian Sea are shown in Figure 14. The heat buildup in the Eurasian Basin over the 16 year model run is approximately 2×10^{19} J/decade and is similar to the warming in the Greenland-Norwegian Sea (Figure 14). The warming in the Amerasian Basin is less than half of that in
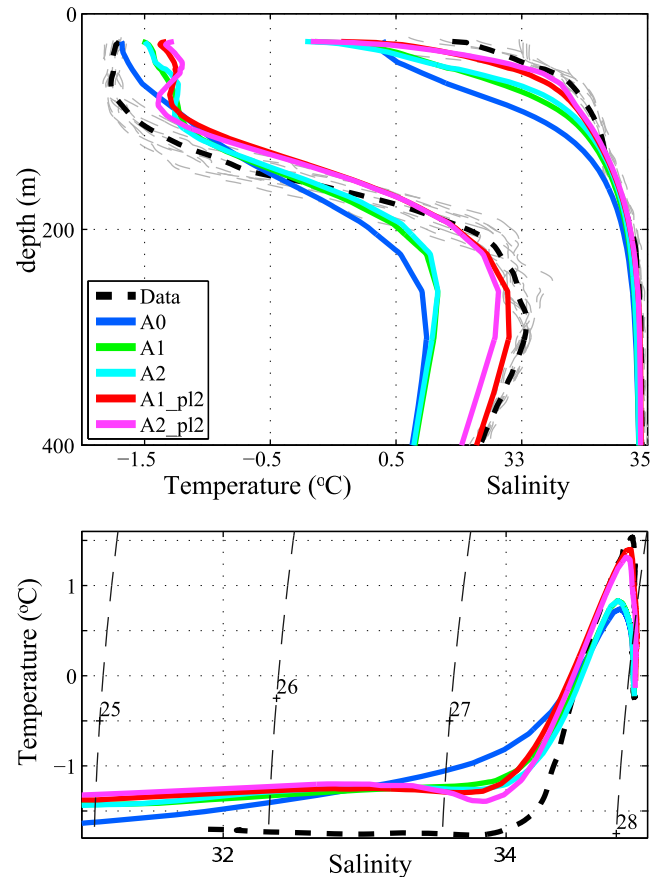

Figure 12. October 2000 vertical temperature and salinity structures in the Amundsen Basin for the experiments listed in Table 1. (top) The actual CTD profiles are shown in gray, with the mean shown in dashed black. (bottom) Dashed contours are density anomaly.
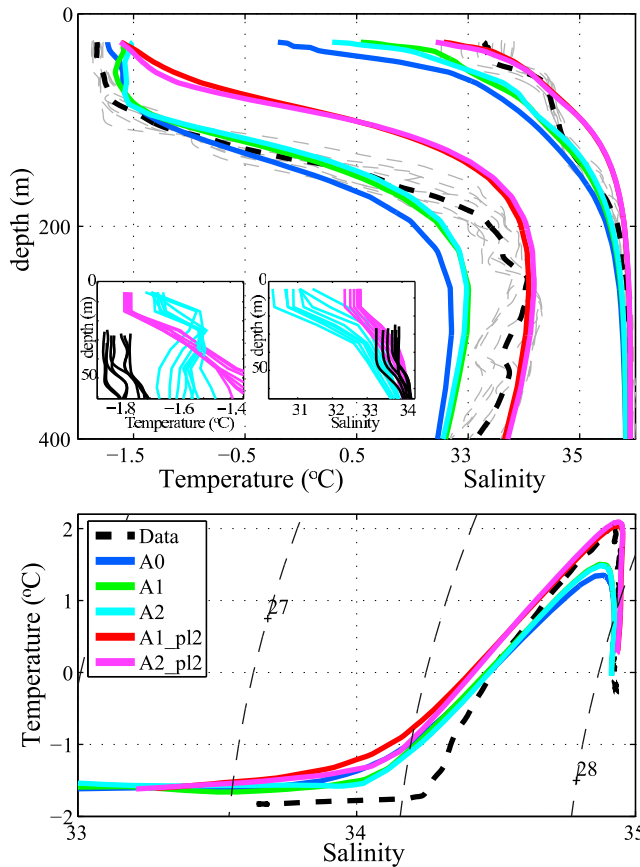
Figure 13. Vertical temperature and salinity structures in the Nansen Basin for October 2000 for the experiments listed in Table 1. (top) The actual CTD profiles are shown in gray, with the mean shown in dashed black. (bottom) Dashed contours are density anomaly. In Figure 13 (top), two insets show the top 50 m of temperature (left inset) and salinity (right inset) for data (black), experiments **A2** (light blue), and **A2_sp2** (magenta). For all values of ν (**A[0-2]**), surface salinity values in the Nansen Basin are significantly fresher by $2-3$ compared to observations. At near-freezing temperature, the salt plume scheme (**A[1-2]_sp[1-2]**) produces more realistic near-surface salinity and hence vertical density structures.

the Eurasian Basin. The drifts in heat content obtained in our model, for both the Amerasian and the Eurasian Basins, are on the lower end of the range reported by *Holloway et al.* [2007] for AOMIP models. Sources for these drifts include model resolution and initial conditions, and a full investigation of the heat drifts is beyond the scope of this study.

7. Summary and Outlook

[32] Subgrid vertical mixing of rejected salt during sea ice formation is implemented in a regional configuration of the MITgcm coupled ocean sea ice model to successfully reproduce the halocline in the Arctic ocean. When a KPP background diffusivity value $\nu \approx 10^{-5}$ m^2/s is used without the salt plume scheme, grid-scale convection is more likely to occur and mixed layer depths exceeding 70 m in the Canada Basin are seen in the solutions. Such deep mixed

layers destroy the halocline and produce unrealistic temperature gradients seen in all basins for our baseline experiment **A0** and in the AOMIP participating models' outputs. Decreasing background diffusivity improves the model fit to data, especially in the Amerasian Basin where a low value of ν is needed to avoid destroying the halocline (M. McPhee, personal communication, 2009). However, over the 14 year model integration period, all values of background diffusivity yield surface salinity values that are unrealistically too fresh in the Eurasian Basin.

[33] Turning on the salt plume scheme reduces the large grid-scale vertical mixing which is an artifact of the model's limited resolution. The scheme takes salt at the surface and distributes it down to the depth of neutral buoyancy and results in a stabilized halocline in the Canada Basin and Chukchi Cap at the end of the 14 year model run. A salt plume scheme with parameters $d\rho/dz = 0.02$ kg/m^3/m and $n = 5$, which correspond to distributing most of the rejected salt to the bottom of the mixed layer, yield the lowest model-data misfits when compared to hydrographic observations in Amundsen, Makarov, and Canada Basins and in the Chukchi Cap. One exception is in the Nansen Basin where our model does not reproduce the observed deep mixed layer. Based on Table 2, a KPP background diffusivity value $\nu = 10^{-6}$ m^2/s in combination with the salt plume scheme works best for our model. This value for ν is consistent with the published value found by *Zhang and Steele* [2007].

[34] *Morison and McPhee* [1998] and M. McPhee (personal communication, 2009) suggest that in the open ocean where sea ice velocity is high, turbulent mixing dominates and mixes the rejected salt during sea ice formation within the mixed layer. We are currently investigating incorporating mixing regimes into the salt plume
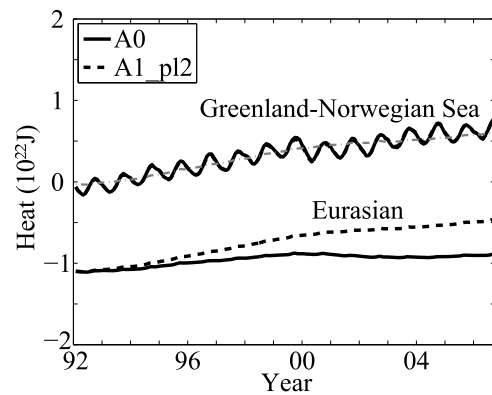

Figure 14. Total heat content in the Eurasian Basin (Nansen and Amundsen combined) and Greenland-Norwegian Sea for the baseline experiment **A0** (black solid line) and salt plume experiment **A1_pl2** (black dashed line). There is no difference in the heat content between the two solutions in the Greenland-Norwegian Sea. The gray dash-dotted line is the heat content of the Eurasian Basin for solution **A1_pl2**, with a vertical offset to match heat content in the Greenland-Norwegian Sea. The heat drifts in both the Greenland-Norwegian Sea and the Eurasian Basin are on the lower end of the range reported by *Holloway et al.* [2007] for AOMIP models.

scheme to produce more realistic vertical mixing processes during brine rejection in the open ocean and along coastal shelves. In addition, we are also investigating the effect of using different numerical tracer background diffusivity values for salinity and temperature on the mixed layer depth and on the cold halocline in our model.

[35] The halocline plays a vital role in regulating heat transport into the mixed layer and in the energy exchange at the ocean sea ice interface. Yet modeling a halocline remains a challenge in current state-of-the-art coupled ocean sea ice models due to missing physics and resolution limitation. This study presents an important contribution to numerical modeling of the Arctic upper ocean. Specifically, we address the problem of the missing halocline, and show that brine rejection at subgrid scale can be used to reproduce and maintain a realistic halocline in our regional configuration of the MITgcm. In addition, we also show the importance of the background diffusivity in the KPP vertical mixing scheme to the mixed layer. Coupled ocean sea ice models with realistic halocline and mixed layer will improve estimates of the ocean sea ice energy exchange at the surface and estimates sea ice mass balance in the Arctic Ocean.

References

Antonov, J., R. Locarnini, T. Boyer, A. Mishonov, and H. Garcia (2006), *World Ocean Atlas 2005*, vol. 2, *Salinity, NOAA Atlas NESDIS*, vol. 62, NOAA, Silver Spring, Md.

Boyd, T., M. Moustafa, and M. Steele (1998), Submarine-based hydrographic observations of the Arctic Ocean, *Data Rep. 165*, Oreg. State Univ., Corvallis, Oreg.

Boyd, T., M. Steele, R. Muench, and J. Gunn (2002), Partial recovery of the Arctic Ocean halocline, *Geophys. Res. Lett.*, *29*(14), 1657, doi:10.1029/2001GL014047.

Bush, J., and A. Woods (1999), Vortex generation by line plumes in a rotating stratified fluid, *J. Fluid Mech.*, *388*, 289–313.

Daru, V., and C. Tenaud (2004), High order one-step monotonicity-preserving schemes for unsteady compressible flow calculations, *J. Comput. Phys.*, *193*(2), 563–594.

Duffy, P., and K. Caldeira (1997), Sensitivity of simulated salinity in a three-dimensional ocean model to upper ocean transport of salt from sea-ice formation, *Geophys. Res. Lett.*, *24*(11), 1323–1326.

Duffy, P., M. Eby, and A. Weaver (1999), Effects of sinking of salt rejected during formation of sea ice on results of an ocean-atmosphere-sea ice climate model, *Geophys. Res. Lett.*, *26*(12), 1739–1742.

Edwards, M., B. Coakley, D. Chayes, S. Okkonen, M. Rognstad, D. Stockwell, and T. Whitledge (1999), Arctic basin insights 1: New data for the Amerasian Basin from SCICEX-99, *Eos Trans. AGU*, *80*(46), Fall Meet. Suppl., Abstract T31F-08.

Helfrich, K. (1994), Thermals with background rotation and stratification, *J. Fluid Mech.*, *259*, 265–280.

Holloway, G., et al. (2007), Water properties and circulation in Arctic Ocean models, *J. Geophys. Res.*, *112*, C04S03, doi:10.1029/2006JC003642.

Hopkins, T., M. Moustafa, C. Kinder, and M. Cook (1998), SCICEX-96 hydrographic data report USS POGY SSN 647 polar cruise 27 August - 12 November 1996, *Tech. Rep. 98-1*, N. C. State Univ., Raleigh, N. C.

Kemp, J., K. Newhall, W. Ostrom, R. Krishfield, and A. Proshutinsky (2005), The Beaufort Gyre Observing System 2004: Mooring recovery and deployment operations in pack ice, *Tech. Rep. WHOI-2005-5*, Woods Hole Oceanogr. Inst., Woods Hole, Mass.

Kozo, T. (1983), Initial model results for Arctic mixed layer circulation under a refreezing lead, *J. Geophys. Res.*, *88*(C5), 2926–2934.

Langseth, M., et al. (1993), SCICEX-93: Arctic cruise of the US navy nuclear powered submarine USS PARGO, *Mar. Technol. Soc. J.*, *27*, 4–12.

Large, W., J. McWilliams, and S. Doney (1994), Ocean vertical mixing: A review and a model with a nonlocal boundary layer parameterization, *Rev. Geophys.*, *32*(4), 363–403.

Locarnini, R. A., A. V. Mishonov, J. I. Antonov, T. P. Boyer, and H. E. Garcia (2006), *World Ocean Atlas 2005*, vol. 1, *Temperature, NOAA Atlas NESDIS*, vol. 62, NOAA, Silver Spring, Md.

Lukas, R., and E. Lindstrom (1991), The mixed layer of the western equatorial Pacific Ocean, *J. Geophys. Res.*, *96*, 3343–3358.

Menemenlis, D., I. Fukumori, and T. Lee (2005), Using Green's functions to calibrate an ocean general circulation model, *Mon. Weather Rev.*, *133*, 1224–1240.

Menemenlis, D., J. M. Campin, P. Heimbach, C. Hill, T. Lee, A. Nguyen, M. Schodlok, and H. Zhang (2008), ECCO2: High resolution global ocean and sea ice data synthesis, *Mercator Ocean Q. Newsl.*, *31*, 13–21.

Morison, J. (1978), The Arctic profiling system, in *Proceedings of the 1978 IEEE First Working Conference on Current Measurement*, vol. 1, pp. 313–318, Univ. of Wash., Seattle, Wash.

Morison, J., and M. McPhee (1998), Lead convection measured with an autonomous underwater vehicle, *J. Geophys. Res.*, *103*(C2), 3257–3281.

Morison, J., M. McPhee, T. Curtin, and C. Paulson (1992), The oceanography of winter leads, *J. Geophys. Res.*, *97*(C7), 11,199–11,218.

Morton, B., S. G. Taylor, and J. Turner (1956), Turbulent gravitational convection from maintained and instantaneous sources, *Proc. R. Soc. London A*, *234*, 1–23.

Muench, R. D., D. C. Smith IV, and C. A. Paulson (1995), Convection beneath freezing leads: New observations compared with numerical model results, *J. Geophys. Res.*, *100*(C3), 4681–4692.

Nakawo, M., and N. Sinha (1981), Growth rate and salinity profile of first-year sea ice in the high Arctic, *J. Glaciol.*, *27*(96), 315–330.

Nguyen, A. T., R. Kwok, and D. Menemenlis (2008), Assessment of the ECCO2 coupled ocean and sea ice solution in the Arctic, paper presented at 2008 Ocean Sciences Meeting, Orlando, Fla.

Rothrock, D., W. Maslowski, D. Chayes, G. Flato, and J. Grebmeier (1999), Arctic Ocean science from submarines: A report based on the SCICEX 2000 workshop, report, Univ. of Wash., Seattle, Wash.

Rudels, B., E. Jones, U. Schauer, and P. Eriksson (2004), Atlantic sources of the Arctic Ocean surface and halocline waters, *Polar Res.*, *23*(2), 181–208.

Scorer, R. (1957), Experiments on convection of isolated masses of buoyant fluid, *J. Fluid Mech.*, *2*(6), 583–594.

Smith, D. C., IV, and J. Morison (1993), A numerical study of haline convection beneath leads in sea ice, *J. Geophys. Res.*, *98*(C6), 10,069–10,083.

Smith, D. C., IV, and J. Morison (1998), Nonhydrostatic haline convection under leads in sea ice, *J. Geophys. Res.*, *103*(C2), 3233–3247.

Smith, D. C., IV, J. Lavelle, and H. Fernando (2002), Arctic Ocean mixed-layer eddy generation under leads in sea ice, *J. Geophys. Res.*, *107*(C8), 3103, doi:10.1029/2001JC000822.

Smith, J. (1974), Oceanographic investigations during the AIDJEX lead experiment, *AIDJEX Bull.*, *27*, 125–133.

Steele, M., and T. Boyd (1998), Retreat of the cold halocline layer in the Arctic Ocean, *J. Geophys. Res.*, *103*(C5), 10,419–10,435.

Turner, J. (1969), Buoyant plumes and thermals, *Annu. Rev. Fluid Mech.*, *1*, 29–44.

Zhang, H., D. Menemenlis, T. Lee, M. Schodlok, D. Volkov, and V. Zlotnicki (2008), Assessment of the ECCO2 high resolution global-ocean and sea-ice synthesis using the CLIVAR/GODAE global synthesis and observations panel metrics, paper presented at 2008 Ocean Sciences Meeting, Orlando, Fla.

Zhang, J., and D. Rothrock (2003), Modeling global sea ice with a thickness and enthalpy distribution model in generalized curvilinear coordinates, *Mon. Weather Rev.*, *131*(5), 681–697.

Zhang, J., and M. Steele (2007), Effect of vertical mixing on the Atlantic Water layer circulation in the Arctic Ocean, *J. Geophys. Res.*, *112*, C04S04, doi:10.1029/2006JC003732.

———————————

R. Kwok, Jet Propulsion Laboratory, California Institute of Technology, MS 300-235, 4800 Oak Grove Dr., Pasadena, CA 91109-8099, USA. (ronald.kwok@jpl.nasa.gov)

D. Menemenlis and A. T. Nguyen, Jet Propulsion Laboratory, California Institute of Technology, MS 300-323, 4800 Oak Grove Dr., Pasadena, CA 91109-8099, USA. (dimitris.menemenlis@jpl.nasa.gov; an.t.nguyen@jpl.nasa.gov)